Tensile properties and strengthening behavior of CoCrFeNiW high entropy alloys with heterogeneous structures

Xue-feng GAO[1], Yao CHEN[1], Hao REN[1], Gang QIN[1], Qi-wen ZHOU[2], Rui-run CHEN[1], Jing-jie GUO[1]

1. National Key Laboratory for Precision Hot Processing of Metals,
Harbin Institute of Technology, Harbin 150001, China;
2. School of Materials Science and Engineering, Shenyang University of Technology, Shenyang 110870, China

Abstract: $Co_{30}Cr_{30}(FeNi)_{40-x}W_x$ (x=0−8 at.%, simplified as HW0−HW8, respectively) high entropy alloys (HEAs) were fabricated by vacuum arc-melting. The microstructure and tensile properties of as-cast and as-annealed alloys were investigated. The results show that HW2 and HW4 have a single FCC phase. The fine and granular μ phase is dispersed in FCC matrix and the area fraction increases with the increase of W content and annealing temperature. The soft FCC matrix and hard μ phase constitute the heterostructure with strain incompatibility. With the increase of W content from 0 to 8 at.%, the yield strength and tensile strength increase from 278 and 629 MPa to 530 and 839 MPa, respectively. The strain maintains 33%. The as-annealed HW8 exhibits superior yield strength (810 MPa) and tensile strength (1087 MPa). The yield strength improvement is attributed to solid-solution, precipitate, and back stress strengthening. Back stress strengthening plays a dominant role in improving tensile strength and plasticity by inducing high hardening behavior in heterogeneous structures.

Key words: high entropy alloy; heterogeneous structure; tensile properties; strain hardening; strengthening mechanism

1 Introduction

High entropy alloy (HEA) with multi-principal elements has been developed as a novel alloy design strategy and potential application material in many fields since it was proposed in 2004 by CANTOR et al [1] and YEH et al [2]. In recent decades, there has been a great deal of interest in the intrinsic characteristics and excellent properties of the HEAs [3−7]. The CoCrFeNi HEA system with a face-centered cubic (FCC) structure exhibits excellent plasticity, corrosion resistance, especially low temperature toughness, and strain hardening ability [8−10]. However, its low yield strength at ambient temperature limits its application as a structural material. Therefore, many strengthening methods have been proposed to improve the yield strength of the FCC HEAs [11−15].

The traditional strengthening methods include solid solution strengthening, grain boundary strengthening, and precipitation strengthening [16−18]. Research has shown that HEAs doped with large-atomic size elements can simultaneously realize the multiple strengthening mechanisms. EIßMANN et al [19] have doped the large atomic size Ti element into CoCrFeMnNi with a FCC structure, which causes high hardness by solid solution strengthening and precipitation strengthening. TEKIN and KOTAN [20] found the improvement of strength as well as thermal stability in the CoCrFeNi alloy by Y and Y_2O_3 additions. SHUN et al [21] reported that the precipitation of hard σ and μ intermetallic phases significantly strengthened the

CoCrFeNiMo$_{0.3}$ HEA and discovered the large lattice distortion due to the Mo element with large atomic size alloying. The addition of transition elements can effectively induce the formation of a topological phase. Although TCP phases can improve the strength, high brittleness can significantly reduce the plasticity of HEAs. It was reported that the content, shape, and distribution of TCP phases are reasonably adjusted, which can effectively utilize the hard property to play an important strengthening role.

At present, more efforts are devoted to obtaining the fine and dispersed hard phase in HEAs, which can hinder the dislocation movement and improve strength and maintain plasticity by increasing the phase interface. The thermo-mechanical methods can effectively adjust the morphology and distribution of the precipitated phases due to the metastable structure. WANG et al [22] have realized the nano-precipitated strengthening of HEAs by annealing treatment. The yield strength of the alloy annealed at 700 °C for 20 h increased significantly by 56%. POLAT et al [23] designed the nano-structured CoCrFeNi HEAs with Y addition by a mechanical alloying process and annealed at various temperatures. The results indicated that Y additions retarded the grain growth and thermal stability to consolidate powders into dense nanocrystalline compact HEAs. TODA et al [24] added Cu and/or Mo to CoCrFe$_2$Ni$_2$ system by aging heat treatments to evaluate thermal stability, and found that Cu and Mo added together improved the stability. FAN et al [25] investigated the phase constituents of four CoCrFeNiX (X=Y, Ti, Zr, and Hf) HEAs after prolonged annealing and the formation of new minor phases at lower temperatures. The as-annealed phases are diverse due to the multi-component characteristics of HEAs. The effects of large atomic size W elements and annealing treatments at high temperatures on phase formation and stability of CoCrFeNi HEAs have rarely been studied.

In this work, the W element with a large atomic size was doped into the non-equimolar Co$_{30}$Cr$_{30}$Fe$_{20}$Ni$_{20}$ HEA with a single-phase FCC structure. The hard phase strengthened Co$_{30}$Cr$_{30}$-(FeNi)$_{40-x}$W$_x$ HEAs were designed and prepared by alloying and adjusting the annealing conditions. The microstructure evolution and tensile properties of as-cast and as-annealed alloys were investigated.

The formation and stability of the precipitated phase were analyzed by thermodynamics. Multiple strengthening mechanisms were discussed. This provides a guide to composition and process designs for improving the properties of HEAs.

2 Experimental

The non-equimolar Co$_{30}$Cr$_{30}$(FeNi)$_{40-x}$W$_x$ ($x=$ 0−8 at.%, hereinafter, simplified as HW0−HW8, respectively) HEAs ingots were fabricated by arc-melting under a Ti-gettered high-purity argon atmosphere. The purity of raw materials with a size of d3 mm × 6 mm was higher than 99.9%. The mixture of pure metals was placed in a water-cooled Cu crucible, then the chamber was first evacuated to ~1×10^{-3} Pa, and then washed twice with high-purity argon to reduce the oxygen content. Before the materials were melted, a titanium ingot was melted to absorb residual oxygen. All ingots (120 g) were repeatedly melted six times to ensure a homogeneous structure. The size of ingots was d60 mm × 10 mm. The as-cast Co$_{30}$Cr$_{30}$(FeNi)$_{32}$W$_8$ ingots were annealed for 2 h at 800, 1000, and 1200 °C (hereinafter, simplified as A800, A1000, and A1200, respectively), and then furnace-cooled in a vacuum furnace (VF−1600 M) under a high-purity argon atmosphere.

The crystal structures were identified by the X-ray diffraction (XRD) with Cu K$_\alpha$ radiation (wavelength λ=0.15406 nm) at the test angles (2θ) of 20°−100°. The scanning rate was 4 (°)/min. The microstructure and chemical composition were observed by scanning electron microscopy (SEM, Merlin Compact) operated at 20 kV with an energy dispersive spectrometer (EDS) and transmission electron microscopy (TEM, FEI Talos F200X). The electron backscattered diffraction (EBSD, Zeiss Super55) measurement with a step size of 0.18 μm was employed to observe the grain size. The SEM and EBSD samples were ground with 3000 grit SiC paper and then mechanically polished with diamond paste (W1.5). Then, the EBSD samples were electro-polished in a mixture solution of HClO$_4$ (~10 vol.%) and C$_2$H$_5$OH (~90 vol.%) with an applied voltage of 25 V for 15−18 s at room temperature. TEM specimens with d3 mm were ground to 45 μm and then fabricated by ion-milling. The EBSD data were analyzed using Channel 5 software.

The tensile samples with a gauge dimension of 15 mm and a cross-section of 2 mm × 1.8 mm were cut into dog-bone shapes by an electric discharge machine. Tensile tests were conducted on an Instron 5569 electronic universal material testing machine at a strain rate of 1×10^{-3} s^{-1} and room temperature. Each tensile sample of the same composition was tested at least three times to acquire reliable results. Tensile loading−unloading− reloading (LUR) tests were performed on an Instron 5569 testing machine. The specimen was first experienced tensile to a 5% strain at a strain rate of 1×10^{-3} s^{-1}, and then was unloaded by the load-control mode to 50 N, followed by reloading to the next unloading strain at the same strain increment (5%) and strain rate (1×10^{-3} s^{-1}).

3 Results and discussion

3.1 Microstructure and phase formation

Figure 1 presents the XRD patterns of as-cast and as-annealed $Co_{30}Cr_{30}(FeNi)_{40-x}W_x$ HEAs. The single FCC solid solution phase is observed in as-cast HW2, HW4, and HW6 in Fig. 1(a). With the increase of W content, a few diffraction peaks of intermetallic phase are observed in as-cast HW8, which is calibrated as μ phase with a hexagonal structure ($a=b$=4.755 Å, c=25.830 Å). When the W content is low, the W atoms are dissolved into the matrix and present a single-phase structure. When W content is further increased, the limited solid solubility of large-sized W atoms (0.1367 nm) in the matrix leads to the formation of the second phase. Figure 1(b) shows the phase structure of as-annealed HW8 at different temperatures. With the increase of annealing temperature, the peak intensity of μ phase increases gradually at 2θ of 37.933°. The crystal plane is calibrated as the (110) plane of μ phase by using PDF#11-0103. The results show that more atoms in this crystal plane are ordered with the increase of annealing temperature due to the thermal drive effect. The 2θ angle of the (311) peak is 89.90°, 90.64°, and 89.98° for A800, A1000, and A1200, respectively. The calculated method of the lattice parameter is applied in CoCrFeNi HEA by (311) peak [26]. The results indicate the FCC matrix phase presents lattice distortion due to the precipitation of μ phase by annealing treatment. The precipitation of μ phase induces the peak to shift to the higher angle to

release lattice distortion energy for A1000. For A1200, the peak shifts to 2θ of 89.98°, which may be attributed to the small amount of μ phase solid solution in the matrix due to the high diffusion driving force of atoms.
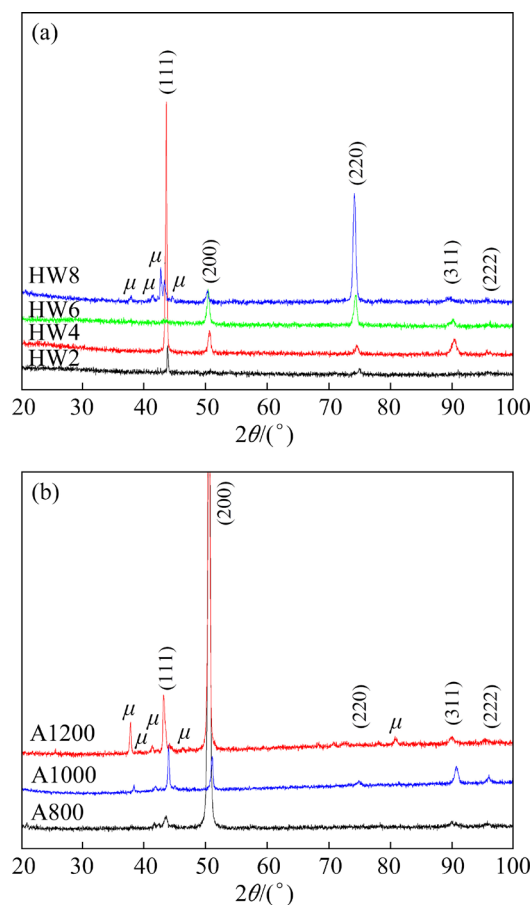

Fig. 1 XRD patterns of $Co_{30}Cr_{30}(FeNi)_{40-x}W_x$ HEAs: (a) As-cast; (b) As-annealed HW8

Figure 2 shows the SEM images of as-cast $Co_{30}Cr_{30}(FeNi)_{40-x}W_x$ HEAs and the upper right corner is a high magnification image. The compositions of the microstructure in as-cast $Co_{30}Cr_{30}(FeNi)_{40-x}W_x$ HEAs are shown in Table 1. As shown in Fig. 2(a), the microstructure of as-cast HW2 is a homogeneous single-phase solid solution. The microstructure is divided into the dendritic (DR) and interdendritic (ID) morphology due to the separation of W atoms in HW4 and HW6, as shown in Figs. 2(b) and (c). The SEM−EDS results indicate that the ID is rich in Cr and W elements. W and Cr elements have a high melting point and a similar electronic structure. W and Cr elements are segregated into the ID during solidification. The dendrite morphology is finer with the increase of W content. A small amount of bright white μ phase
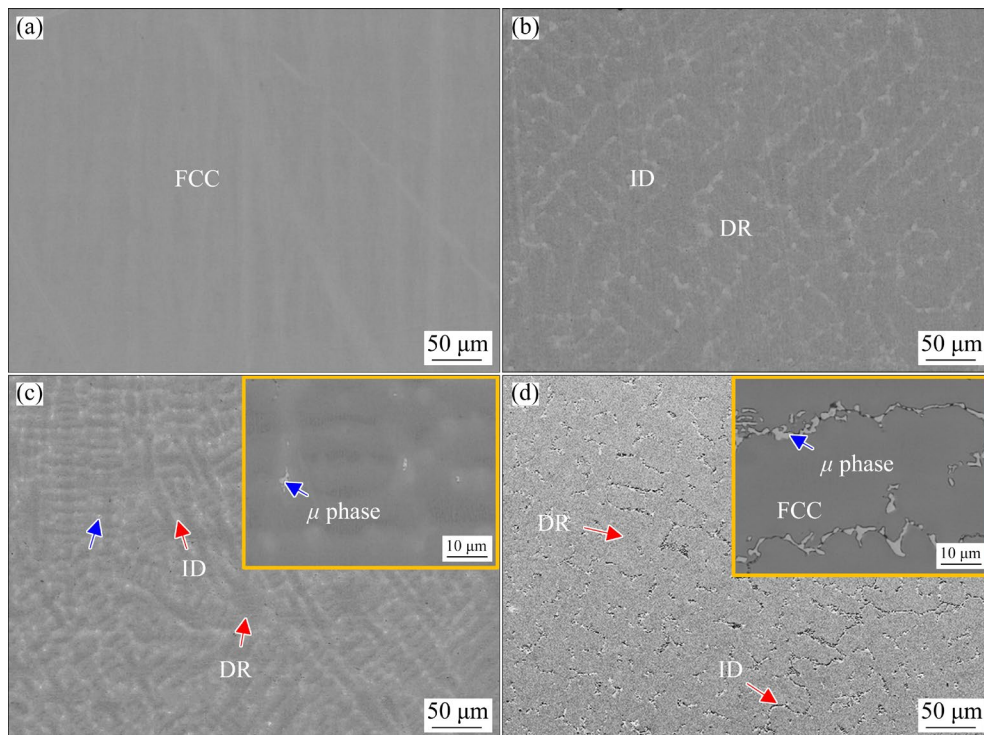
Fig. 2 Microstructure of as-cast $Co_{30}Cr_{30}(FeNi)_{40-x}W_x$ HEAs: (a) HW2; (b) HW4; (c) HW6; (d) HW8 (Upper right corner is a high magnification image)

Table 1 Compositions of as-cast $Co_{30}Cr_{30}(FeNi)_{40-x}W_x$ HEAs from SEM−EDS analysis as marked in Fig. 2

Alloy	Region	Content/at.%				
		Co	Cr	Fe	Ni	W
HW2	FCC	30.58	29.36	19.28	18.80	1.97
HW4	DR	30.01	30.24	18.32	17.54	3.89
	ID	26.05	35.84	16.05	15.54	6.52
HW6	DR	31.03	28.37	17.88	17.19	5.53
	ID	29.51	30.69	16.93	16.72	6.15
	μ phase	22.68	29.94	14.80	14.08	18.50
HW8	FCC	29.83	30.57	15.94	16.10	7.56
	μ phase	20.45	23.83	9.20	7.67	38.85

rich in W element is observed in ID of HW6 alloy, as shown in the high magnification image of Fig. 2(c) and Table 1. In HW8, W content is high, and a large amount of W (38.85 at.%) segregates to completely form μ phase in ID, as shown in Fig. 2(d). TEKIN et al [27] prepared the nanocrystalline $(CoCrFeNi)_{100-x}Zr_x$ HEAs by high energy mechanical alloying and found in-situ formed oxide in the matrix. To further observe the composition of precipitates, the elemental distribution maps of HW8 are shown in Fig. 3. The results show that the μ phase is rich in W elements.

The Cr and O elements are not observed in precipitates. The microstructure is composed of the FCC matrix phase and μ precipitate phase, which corresponds to the XRD results. The FCC phase is a metastable structure and μ phase is stable for $Co_{30}Cr_{30}(FeNi)_{40-x}W_x$ HEAs by thermodynamic analysis.

To further analyze the microstructure of the alloys with the low amount of W, TEM characterization of HW2 is shown in Fig. 4. The bright field (BF) image shows that HW2 has a single-phase structure without observing the second phase in Fig. 4(a). Figure 4(b) shows the EDS compositional images of the FCC phase, which indicates that the single-phase structure has a uniform composition in HW2. The selected area diffraction pattern (SADP) of the FCC phase is characterized in Fig. 4(c), which is calibrated by the [310] zone axis. The result is consistent with the XRD and SEM results.

To study FCC matrix and μ phase stability of $Co_{30}Cr_{30}(FeNi)_{40-x}W_x$ HEAs, the microstructure of HW8 is observed at various annealing temperatures, as shown in Fig. 5. The chemical compositions determined by SEM−EDS analysis are summarized in Table 2. For A800, the primary μ phase at the
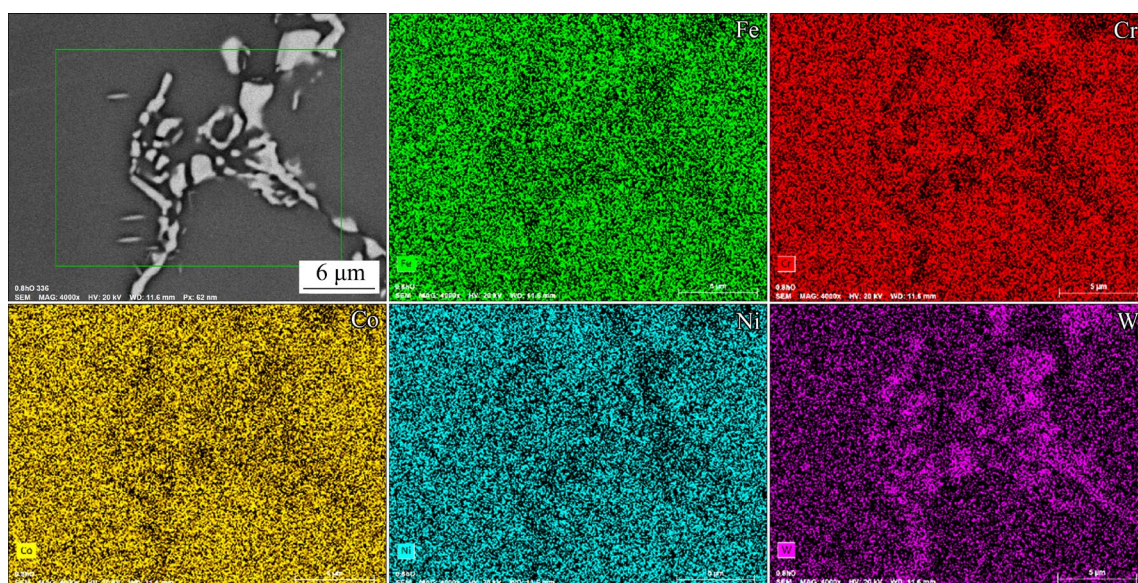
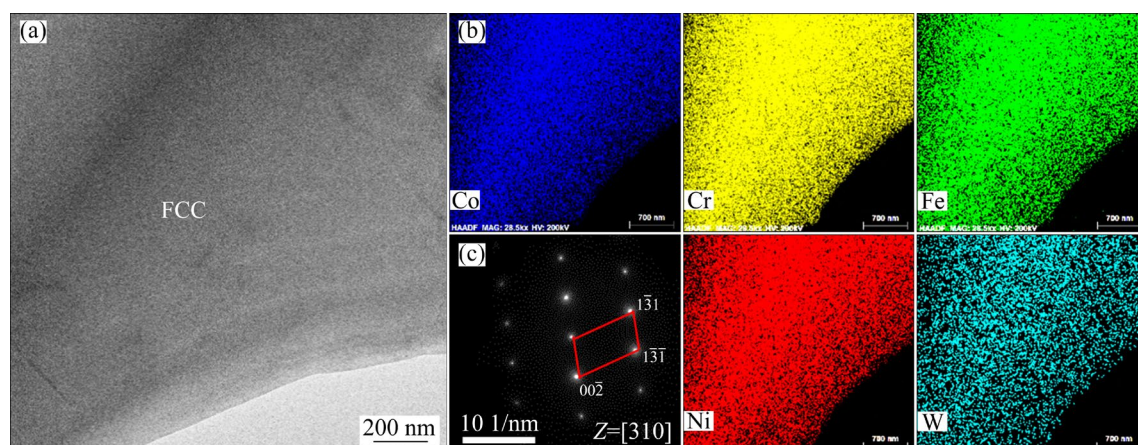**Fig. 3** Elemental distribution maps of HW8

Fig. 4 TEM analysis results of FCC phase in HW2: (a) Bright field TEM image; (b) EDS compositional images; (c) Selected area diffraction patterns

grain boundary disperses and the fine strip μ phase precipitates near the primary phase, as shown in Figs. 5(a) and (b). The results indicate that the primary μ phase is dissolved into the FCC matrix and the W element diffuses to form the fine annealed μ phase due to the thermal driving force of the annealing treatment. The new phase constrained by the surrounding matrix cannot freely expand to produce elastic strain energy, which causes the strip shape with lower elastic strain energy. For A1000, the μ phase is rich in W elements and dispersed in the FCC matrix, as shown in Fig. 5(c) and Table 2. The primary μ phase is dissolved further. The fine strip μ phase increases and grows, as shown in Fig. 5(d). With the further increase of annealing temperature, the annealed μ phase in A1200 is

spheroidized and dissolved due to the high temperature driving force. The dispersed particles are uniformly distributed in the FCC matrix, as shown in Figs. 5(e) and (f). A large number of μ phases rich in W elements are precipitated and dissolved to cause lattice distortion of the FCC matrix, which corresponds to the results of XRD in Fig. 1(b). The results induce solid solution strengthening and precipitate strengthening to improve the mechanical properties.

The W alloying and annealing temperature of $Co_{30}Cr_{30}(FeNi)_{40-x}W_x$ HEAs have a significant impact on the formation and stability of μ phase. HEAs tend to form microstructures with thermo-dynamic stability by minimizing Gibbs free energy change (ΔG_{mix}) at a certain driving force [28,29]. To
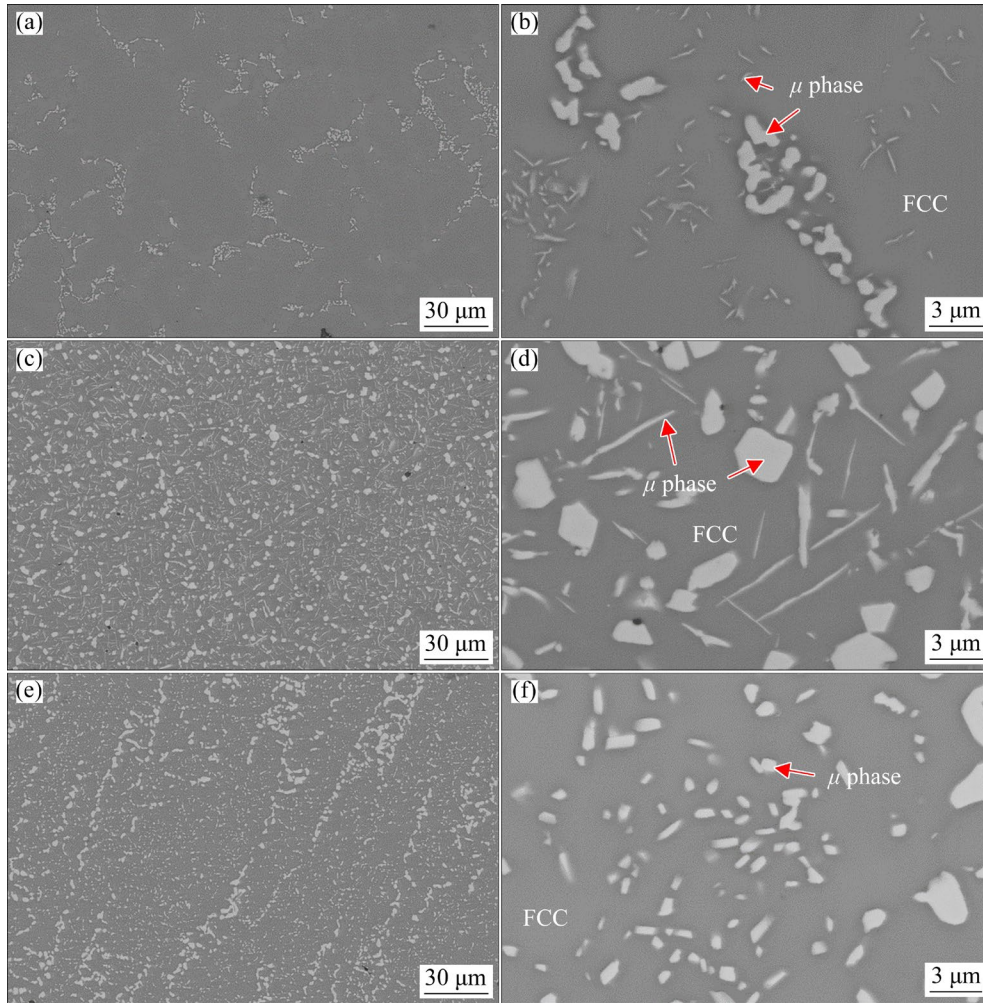
Fig. 5 Backscattered electron (BSE) SEM images of as-annealed HW8 at various temperatures: (a, b) A800; (c, d) A1000; (e, f) A1200

Table 2 Compositions of as-annealed HW8 from SEM−EDS analysis as marked in Fig. 5

Sample	Phase	Content/at.%				
		Co	Cr	Fe	Ni	W
A800	FCC	29.79	30.88	15.96	15.80	7.57
	μ phase	30.74	27.38	11.02	7.65	30.74
A1000	FCC	30.91	31.08	16.97	16.91	4.13
	μ phase	26.18	27.15	12.83	10.51	23.33
A1200	FCC	30.38	31.19	16.56	16.82	5.05
	μ phase	25.42	24.57	12.39	8.68	28.94

discuss the effect of W element on the phase formation and stability of $Co_{30}Cr_{30}(FeNi)_{40-x}W_x$ alloy during solidification, the formation Gibbs free energy change (ΔG_{mix}^0) of the as-cast FCC phase and μ phase is calculated by Eq. (1), based on the chemical compositions of different microstructure in Table 1. The transformation Gibbs free energy change (ΔG_{mix}^*) of the phase in HW8 at different annealing temperatures is calculated by Eq. (2) [30]. The thermodynamic parameters of enthalpy change of mixing (ΔH_{mix}), entropy change of mixing (ΔS_{mix}), and melting point for different phases are calculated by Eqs. (3)−(5) [31−34]:

$$\Delta G_{mix}^0 = \Delta H_{mix} - T_m \Delta S_{mix} \tag{1}$$

$$\Delta G_{mix}^* = \Delta H_{mix} - T_A \Delta S_{mix} \tag{2}$$

$$\Delta H_{mix} = \sum_{i=1,i\neq j}^{n} 4 \Delta H_{ij}^{mix} c_i c_j \tag{3}$$

$$\Delta S_{mix} = -R \sum_{i=1}^{n} c_i (\ln c_i) \tag{4}$$

$$T_m = \sum_{i=1}^{n} c_i (T_m)_i \tag{5}$$

where T_m is the melting point of phases with the chemical composition in Table 1, T_A denotes the as-annealed temperature, n is the number of component elements, c_i is the molar fraction of the ith component, R is the molar gas constant being 8.314 J/(mol·K), ΔH_{ij}^{mix} is the enthalpy change value of mixing between the ith and jth components, $(T_m)_i$ is the melting point of the ith component, as shown in Table 3 [32,33].

The calculated thermodynamic parameters of different phases in the as-cast and as-annealed $Co_{30}Cr_{30}(FeNi)_{40-x}W_x$ HEAs are summarized in Tables 4 and 5, respectively. The Gibbs free energy change of phases in $Co_{30}Cr_{30}(FeNi)_{40-x}W_x$ HEAs is shown in Fig. 6. The FCC, ID, and μ phase of as-cast $Co_{30}Cr_{30}(FeNi)_{40-x}W_x$ HEAs have different ΔG_{mix}^0 due to component differences during solidification in Fig. 6(a). With the addition of the W element, the Gibbs free energy change of different structures decreases. The results indicate that W elements can improve the phase formation ability. As shown in Fig. 6(a), the FCC phase exhibits the highest ΔG_{mix}^0, the ID has the medium ΔG_{mix}^0, and μ phase exhibits the lowest ΔG_{mix}^0. The results indicate that the FCC phase has a metastable structure and μ phase has a stable structure. The well-known CoCrFeMnNi HEA considered as a metastable FCC phase structure [35].

Table 3 Melting point ($(T_m)_i$) of ith component and enthalpy values of mixing (ΔH_{ij}^{mix}) between the ith component and jth component in binary equimolar alloys [32,33]

Element	ΔH_{ij}^{mix}/(kJ·mol^{-1})				
	Co (T_m=1494.85 °C)	Cr (T_m=1906.85 °C)	Fe (T_m=1537.85 °C)	Ni (T_m=1454.85 °C)	W (T_m=3410.85 °C)
Co	−	−4	−1	0	−1
Cr	−4	−	−1	−7	1
Fe	−1	−1	−	−2	0
Ni	0	−1	−2	−	−3
W	−1	1	0	−3	0

Table 4 Thermodynamic parameters of different phases in as-cast $Co_{30}Cr_{30}(FeNi)_{40-x}W_x$ HEAs

Alloy	Structure	ΔH_{mix}/(kJ·mol^{-1})	T_m/°C	ΔS_{mix}/(J·mol^{-1}·K^{-1})	ΔG_{mix}/(kJ·mol^{-1})
HW2	FCC	−3.01292	1927.302	11.89797	−29.1927
HW4	DR	−2.84181	1967.983	12.18352	−30.1449
	ID	−2.49855	2041.27	12.29748	−30.9582
HW6	DR	−2.78701	1991.652	12.39715	−30.8622
	ID	−2.68572	2012.869	12.42043	−31.0772
	μ phase	−2.14798	2246.545	13.04071	−35.0046
HW8	FCC	−2.58227	2039.2122	12.51354	−31.5162
	μ phase	−1.19694	2611.065	12.05643	−35.9684

Table 5 Thermodynamic parameters of different phases in as-annealed HW8 HEAs

Alloy	Structure	ΔH_{mix}/(kJ·mol^{-1})	ΔS_{mix}/(J·mol^{-1}·K^{-1})	ΔG_{mix}/(kJ·mol^{-1})
A800	FCC	−3.56727	12.49935	−16.9791
	μ phase	−2.58028	12.63372	−15.9921
A1000	FCC	−3.74255	12.13236	−19.187
	μ phase	−2.60298	12.84191	−18.95017
A1200	FCC	−3.71597	12.25054	−19.8325
	μ phase	−2.24153	12.66028	−18.3581
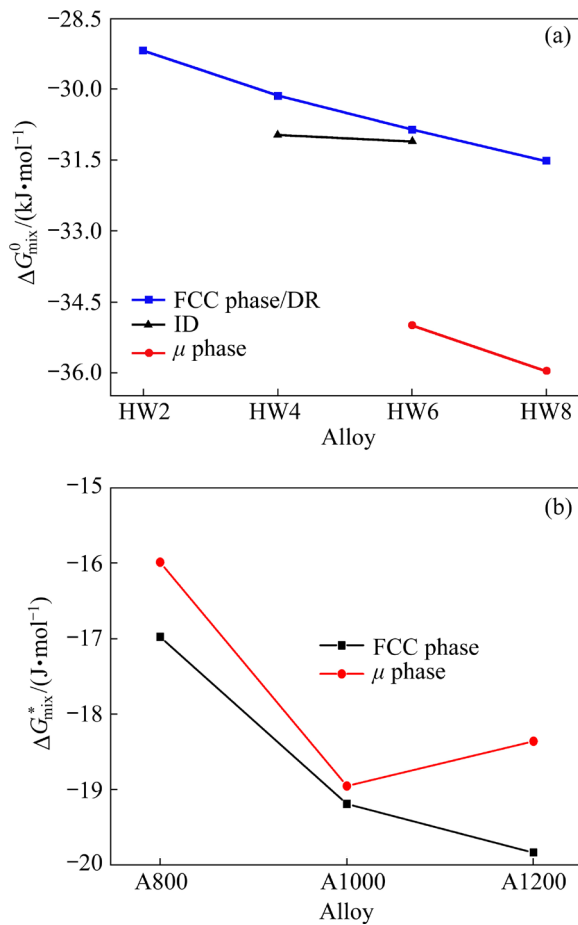
Fig. 6 Gibbs free energy changes of phases in $Co_{30}Cr_{30}(FeNi)_{40-x}W_x$ HEA: (a) Phase formation ΔG_{mix}^0 in as-cast alloys; (b) Phase transformation ΔG_{mix}^* of HW8 during annealing treatment

At a certain driving force, the alloys tend to form a stable structure during solidification [36,37]. With the increase of W content, the metastable FCC phase precipitates to become μ phase with a stable structure. The hard μ phase enhances the strength by hindering dislocation movement.

The stability of the intermetallic phase depends on temperature. The transformation Gibbs free energy change ΔG_{mix}^* of μ phase in HW8 at different annealing temperatures is depicted in Fig. 6(b). The ΔG_{mix}^* of μ phase is higher than that of the FCC matrix phase, which indicates that the μ phase is unstable at annealing temperatures. The content and morphology of μ phase are adjusted by appropriate heat treatment temperatures according to the thermodynamic factors, as shown in Fig. 5. With the increase of annealing temperature, the ΔG_{mix}^* of μ phase decreases first, and then increases. The ΔG_{mix}^* of μ phase is the lowest at A1000, which induces a greater driving force of

precipitation and growth to disperse in the FCC matrix. For A1200, the ΔG_{mix}^* increases slightly, which indicates that the μ phase is unstable due to W atoms diffusion at high temperatures compared with that of A1000. The strip shape with a smaller elastic strain energy transforms into a nearly spherical shape by thermal drive force of A1200. The formation and stability of μ phase play an important role in the mechanical properties of $Co_{30}Cr_{30}(FeNi)_{40-x}W_x$ HEAs.

3.2 Mechanical properties and strengthening mechanisms

Figure 7 shows the tensile engineering stress−strain curves of the as-cast and as-annealed $Co_{30}Cr_{30}(FeNi)_{40-x}W_x$ HEAs. The effect of the W element on the mechanical properties of as-cast $Co_{30}Cr_{30}(FeNi)_{40-x}W_x$ HEAs is shown in Fig. 7(a). With the increase of W content from 0 to 8 at.%, the yield strength gradually increases from 278 to 530 MPa for HW0 and HW8. The fracture strain
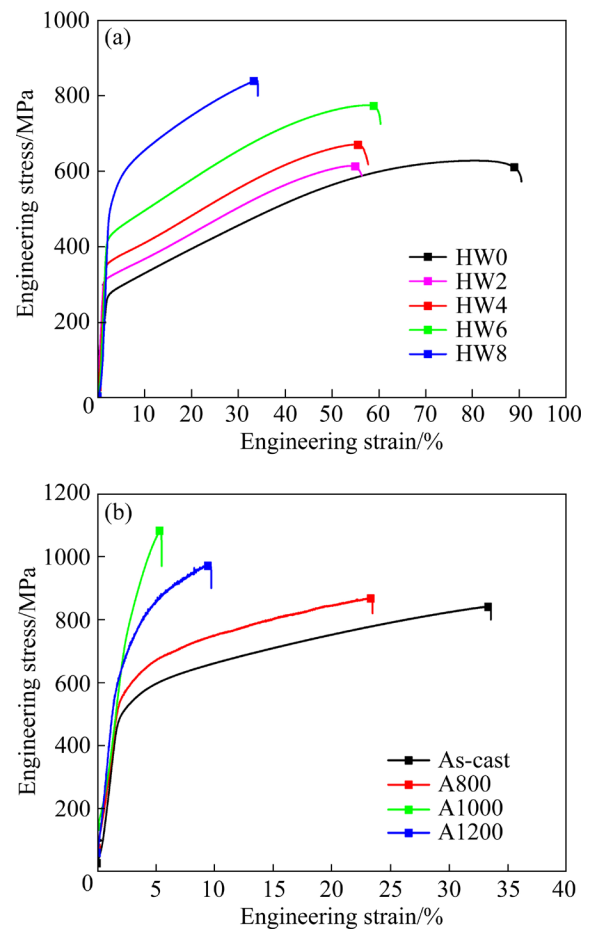

Fig. 7 Tensile engineering stress−strain curves of $Co_{30}Cr_{30}(FeNi)_{40-x}W_x$ HEAs: (a) As-cast; (b) As-annealed HW8

increases first, then decreases, and finally increases again. The yield strength of HW8 is 68.8% higher than that of HW2 with a single FCC phase. The improvement of yield strength is attributed to the μ phase precipitation. HW2 and HW4 exhibit nearly similar plasticity of 55% and 56%, respectively. The yield strength and tensile strength in HW4 are 347 and 670 MPa, respectively. In HW6, the tensile strength is 772 MPa and the fracture strain increases to 59%. HW8 has a high tensile strength of 839 MPa and maintains a plasticity of 33%. The improvement of plasticity is related to the hard phase and soft phase heterostructures. The fracture morphologies of the as-cast $Co_{30}Cr_{30}(FeNi)_{40-x}W_x$ HEAs after tensile deformation are shown in Fig. 8. A large number of dimples are observed in HW2−HW6, as shown in Figs. 8(a−c). The dimples with large and deep morphology imply high plasticity. In HW6, the small and shallow dimples are observed in Fig. 8(c), which indicates the high tensile strength. In HW8, a few dimples and typical intergranular fracture morphology are observed in Fig. 8(d), which cause the ductile and brittle mixed fracture.

The engineering stress−strain curves of the as-annealed HW8 are shown in Fig. 7(b). The strength increases and the plasticity decreases in the as-annealed alloy compared with the as-cast HW8.

At A800, the yield strength, tensile strength, and fracture strain are 561 MPa, 867 MPa, and 23%, respectively. The yield strength of A800 significantly increases to 814 MPa, which is an increase of 44.4% compared with that of A800. The tensile strength of A1000 is 1087 MPa, and the plasticity decreases to 5.3%. A large number of μ phase precipitates improve the strength of HW8 during annealing. For A1200, the yield and tensile strengths decrease to 654 and 970 MPa, respectively, and the plasticity increases to 10%. The plasticity has increased by 88.68% compared with that of A1000. The dissolution and spheroidization of μ phase improve the plasticity of the alloy at high temperatures. The results further illustrate that the properties of $Co_{30}Cr_{30}(FeNi)_{40-x}W_x$ HEAs can be improved by adjusting the phase distribution and morphology during annealing process.

The addition of W element and annealing treatment can improve the strength and maintain the applicable plasticity in $Co_{30}Cr_{30}(FeNi)_{40-x}W_x$ HEAs, which is attributed to the μ phase precipitation. The μ phase areal fraction is determined from microstructure images by utilizing the ImageJ analysis, as shown in Fig. 9(a). In as-cast HW6 and HW8, the μ phase areal fraction is 0.167% and 7.788%, respectively. W element with large atomic
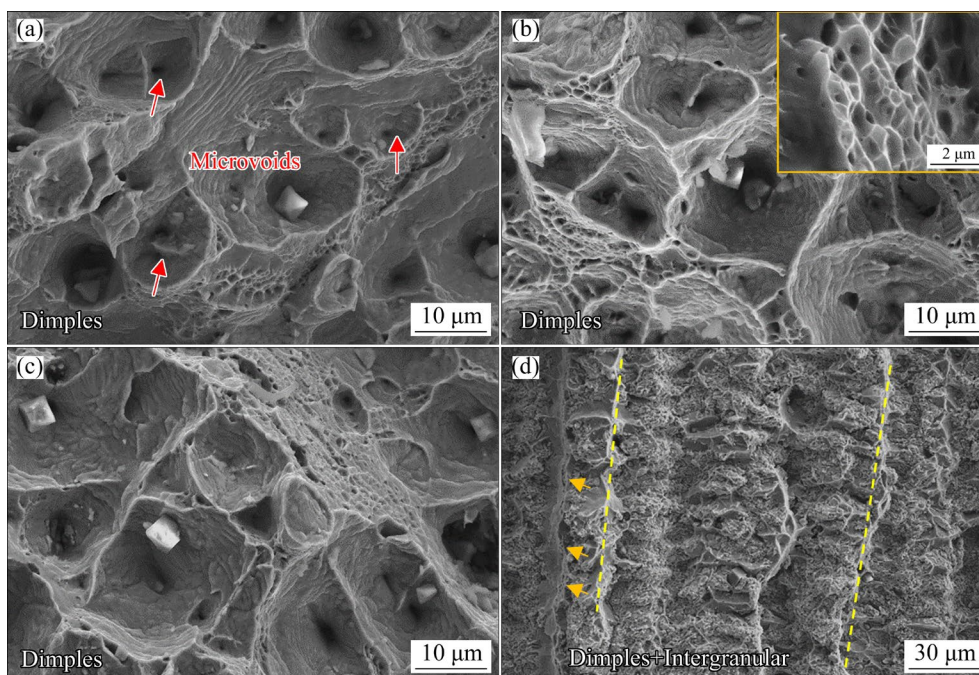

Fig. 8 Fracture morphologies of $Co_{30}Cr_{30}(FeNi)_{40-x}W_x$ HEAs: (a) HW2; (b) HW4; (c) HW6; (d) HW8 (Upper right corner is high magnification image of dimples)

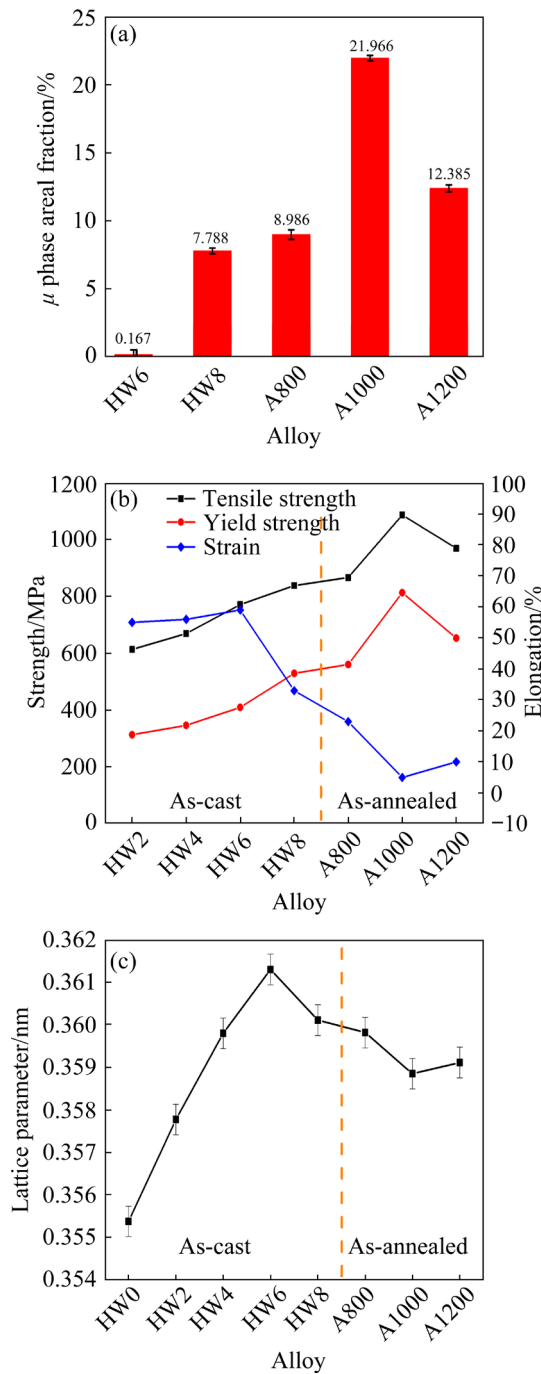**Fig. 9** Tensile properties and lattice parameters of as-cast $Co_{30}Cr_{30}(FeNi)_{40-x}W_x$ HEAs and as-annealed HW8: (a) μ phase areal fraction; (b) Strength and elongation; (c) Lattice parameters of FCC phase

sizes is added to promote μ phase formation. After annealing at different temperatures, the μ phase is further precipitated. For A800, a lower thermal drive force induces the area fraction to increase from 7.788% to 8.986%. For A1000, the area fraction of μ phase significantly increases to 21.966% due to the high thermal driving force. For A1200,

the area fraction of μ phase decreases to 12.385% due to phase dissolution by atomic diffusion at a higher driving force. The trend of strength in as-cast and as-annealed alloys is consistent with that of μ phase area fraction and is summarized in Fig. 9(b). With the precipitation of μ phase, the increment in yield strength significantly increases. The yield strength of HW4 is 10.5% higher than that of HW2. The yield strength of HW6 is 18.2% higher than that of HW4, and the yield strength of HW8 is 20.2% higher than that of HW6.

The lattice parameters of FCC matrix in as-cast and as-annealed $Co_{30}Cr_{30}(FeNi)_{40-x}W_x$ HEAs are calculated by utilizing XRD peaks and summarized in Fig. 9(c). With the increase of W content, the solid solution of W elements with a large atomic size into an alloy with a single FCC phase induces large lattice distortion, resulting in solid solution strengthening. Figure 10 shows the grain morphologies of as-cast $Co_{30}Cr_{30}(FeNi)_{40-x}W_x$ HEAs by EBSD test. The results show that the grain size of HW2 and HW4 is similar, approximately 200 μm in Figs. 10(a) and (b), respectively. With the increase of W content, the grain size is about 150 μm in HW6 and HW8, as shown in Figs. 10(c) and (d), respectively. The μ phase precipitates at the grain boundary to inhibit the grain growth, but the influence is weak. The grain boundary strengthening effect has a low contribution to the improvement of yield strength. The improvement in yield strength in HW2 and HW4 is attributed to the solid solution strengthening.

HW6 has the largest lattice parameter. A small amount of μ phase precipitates in the ID of HW6. In the solidification process, the liquid phase of five
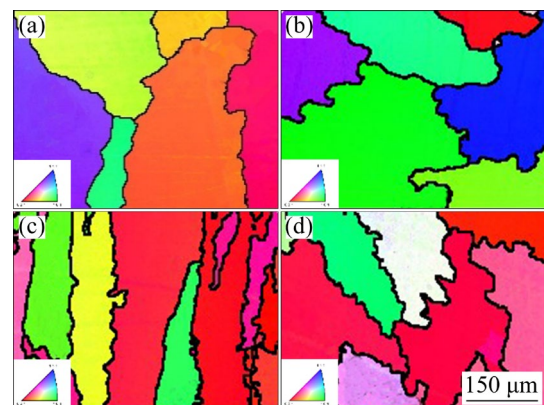

Fig. 10 Inverse pole figure (IPF) maps of as-cast $Co_{30}Cr_{30}(FeNi)_{40-x}W_x$ HEAs: (a) HW2; (b) HW4; (c) HW6; (d) HW8

elements at high temperature solidifies to form the FCC matrix due to the mutual solution. The FCC matrix has a metastable CoCrFeNiW chemical composition and a supersaturated solid solution due to the rapid cooling effect of the water-cooled copper crucible. As the solidification temperature decreases, W atoms show limited solid solubility in the FCC matrix due to the large atomic size (0.1363 nm). The segregation of solute from the residual liquid leads to W elements partitioning towards ID. The yield strength improvement of HW6 is mainly attributed to solution strengthening and precipitation strengthening.

With the increase of W content in HW8, a large amount of W element precipitates in ID during solidification and completely forms μ phase and the lattice parameter decreases. The solution strengthening effect decreases due to W segregation in μ phase. The precipitation and growth of μ phase consume W atoms from the FCC matrix, which causes the tradeoff relationship between solution strengthening and precipitation strengthening [38]. The hard μ phase hinders dislocation slip. The precipitation strengthening mechanism plays a dominant role in improving the yield strength of as-cast and as-annealed HW8. It can be seen from the increment in yield strength that the precipitation phase has a more significant strengthening effect. The precipitation strengthening effect (σ_p) from μ phase is quantified using Orowan mechanism by Eqs. (6)−(8) as follows [39,40]:

$$\sigma_p = M \frac{0.4 Gb}{\pi \lambda} \frac{\ln(\frac{2\overline{r}}{b})}{\sqrt{1-v}} \qquad (6)$$

$$b = \frac{\sqrt{3}a}{2} \qquad (7)$$

$$\lambda = \left(\sqrt{\frac{3\pi}{4f}} - 1.64 \right) \overline{r} \qquad (8)$$

where M(=3.06) is the Taylor factor; G(=86.12 GPa) is the shear modulus by JMatPro using a stainless steel database (the shear modulus of the equimolar CoCrFeNi HEA is calculated to be 84.87 GPa by the same calculation method, which corresponds to other simulation and experimental results (84 GPa) [41]); b is the amplitude of Burgers vector calculated by Eq. (7), a(=0.36011 nm) is a lattice parameter; $\overline{r}$ is the mean radius of precipitates measured by ImageJ software; λ is the edge-to-edge

inter-precipitates spacing calculated by Eq. (8), f(=7.788%) is the volume fraction of the precipitate; v=0.3 is the Poisson's ratio. The σ_p is calculated to be 123.57 MPa, which is less than the yield strength (530 MPa). Back stress generated by the heterogeneous phase has a significant effect on improving the strength and plasticity of HEAs [3,42,43].

Figure 11 shows the deformed surface morphologies of HW8 after a tensile fracture. The cracks initiate in the hard μ phase and are passivated by the soft matrix phase to delay propagation. The width of cracks is measured by utilizing ImageJ analysis. The cracks have an average width of (203±86) nm, and single or bifurcated propagation paths of the cracks are observed in as-cast HW8, as shown in Fig. 11(b). In as-annealed HW8 at 1000 °C, the cracks have a width of (130±51) nm, and the propagation paths of the cracks are single, as shown in Fig. 11(d). During the tensile deformation, the stress is concentrated at the phase interface. The dislocations cut through the hard particles to produce cracks. The cracks are wider due to the FCC matrix deformation. The heterogeneous structure of the soft FCC phase and the hard μ phase induces the formation of back stress in the FCC matrix.

Figure 12 shows the stress partition behavior of as-cast HW8 with μ phase. The loading−unloading−reloading (LUR) tensile curve exhibits an obvious hysteresis loop in each unloading−reloading cycle, as shown in Fig. 12(a). The hysteresis loops are more obvious with the increase of the strain during the unloading and reloading, which indicates the back stress strengthening effect. In heterogeneous structures, the flow stress (σ_{flow}) is divided into the back stress (σ_{back}) and effective stress (σ_{eff}) [44]. The back stress and effective stress can be calculated by Eqs. (9) and (10) respectively as follows [45]:

$$\sigma_{back} = \frac{\sigma_r + \sigma_u}{2} \qquad (9)$$

$$\sigma_{eff} = \sigma_{flow} - \sigma_{eff} \qquad (10)$$

where σ_r is the reloading yield stress and σ_u is the unloading yield stress, as shown in Fig. 12(a). The calculated results are shown in Fig. 12(b). The σ_{back} and σ_{eff} increase with the increase of strain. The σ_{eff} impedes dislocation movement, which improves the strength during tensile deformation. The σ_{back} is
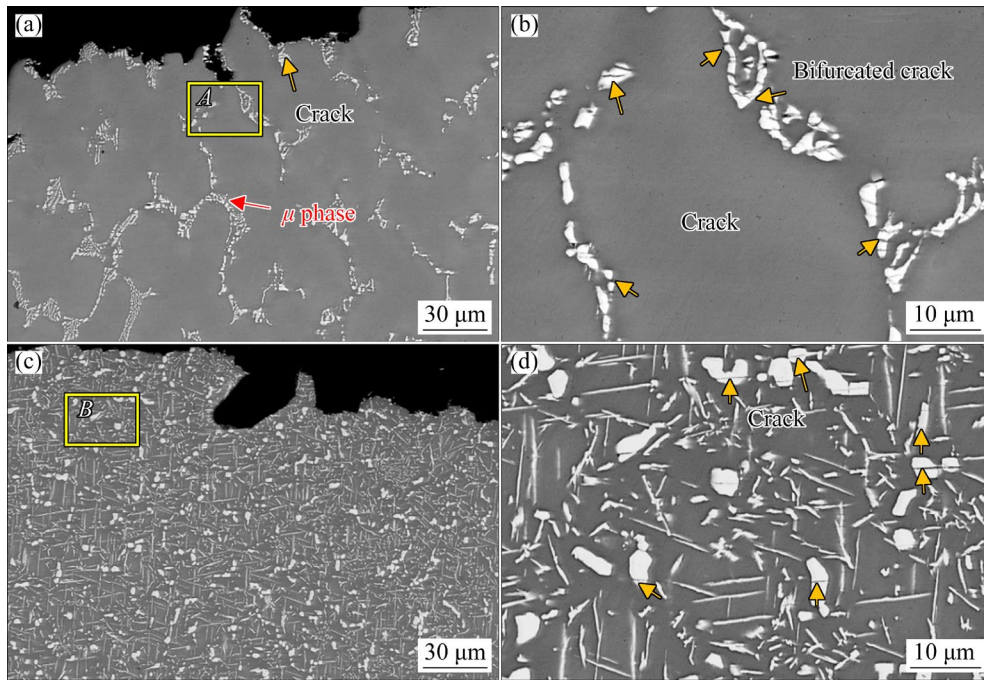
Fig. 11 Deformed surface morphologies of HW8 after tensile fracture: (a, b) As-cast; (b) High magnification image of Region *A* in (a); (c, d) A1000; (d) High magnification image of Region *B* in (c)
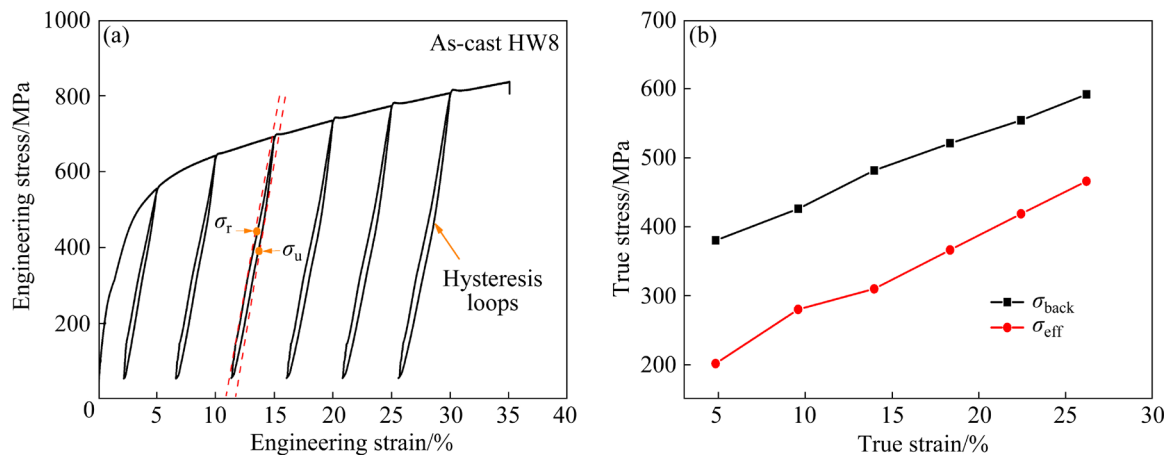

Fig. 12 Stress partition behavior of heterogeneous structures: (a) Loading−unloading−reloading (LUR) engineering stress−strain curve; (b) Evolution of σ_{back} and σ_{eff} with change of true strain

380.22 MPa at strain near the yield point, which indicates that the back stress has a great contribution to the improvement of yield strength. The yield strength (530 MPa) includes the back stress of 380.22 MPa, precipitation strengthening of 123.57 MPa, and solution strengthening of 26.21 MPa. The σ_{back} is generated in the soft FCC matrix, which induces the high strain hardening behavior to maintain good ductility at a high stress level. The FCC phase with high strain hardening ability passivates the cracks, which leads to high plasticity in the heterogeneous structural alloys.

Back stress strengthening plays a dominant role in improving strength and preserving plasticity in $Co_{30}Cr_{30}(FeNi)_{40-x}W_x$ HEAs.

4 Conclusions

(1) The microstructure is composed of the FCC matrix phase and μ precipitate phase in as-cast $Co_{30}Cr_{30}(FeNi)_{40-x}W_x$ HEAs with the increase of W content. In as-cast HW8, the μ phase area fraction is 7.788%. In as-annealed HW8, the fraction of μ phase reaches a maximum of 21.966% at 1000 °C.

The fine strip and granular μ phase are dispersed in the FCC matrix.

(2) The μ phase exhibits the lowest Gibbs free energy change by thermodynamic calculation, which is conducive to precipitate from the metastable FCC phase. The soft FCC matrix and hard μ phase constitute a heterostructure with strain incompatibility.

(3) The yield strength of as-cast alloys gradually increases from 278 to 530 MPa with the increase of W content from 0 to 8 at.%. The as-cast HW8 has a tensile strength of 839 MPa and maintain a strain of 33%. In as-annealed HW8 at 1000 °C, the yield strength and tensile strength present maximum values of 814 and 1087 MPa, respectively.

(4) The yield strength improvement is mainly attributed to solution strengthening, precipitation strengthening, and back stress strengthening. The heterostructure induces the σ_{back} formation in the soft FCC matrix, which induces the high strain hardening behavior to maintain good ductility at a high stress level. This work offers an approach to design high-performance heterostructure materials with great application potentials.

CRediT authorship contribution statement

Xue-feng GAO: Conceptualization, Executor of the experiment, Data curation, Writing − Original draft; **Yao CHEN:** Data curation, Supervision; **Hao REN:** Supervision, Investigation; **Gang QIN:** Formal analysis, Investigation; **Qi-wen ZHOU:** Formal analysis, Investigation, Funding acquisition; **Rui-run CHEN:** Project administration, Designing experiment, Investigation, Funding acquisition; **Jing-jie GOU:** Project administration, Funding acquisition.

Declaration of competing interest

The authors declare that they have no known competing financial interests or personal relationships that could have appeared to influence the work reported in this paper.

References

[1]   CANTOR B, CHANG I T H, KNIGHT P, VINCENT A J B. Microstructural development in equiatomic multicomponent alloys [J]. Materials Science and Engineering: A, 2004, 375/376/377: 213−218.

[2]   YEH J W, CHEN S K, LIN S J, GAN J Y, CHIN T S, SHUN T T, TSAU C H, CHANG S Y. Nanostructured high-entropy alloys with multiple principal elements: Novel alloy design concepts and outcomes [J]. Advanced Engineering Materials, 2004, 6(5): 299−303.

[3]   ZHU Cheng-yan, WU Hao, ZHU He-guo, LI Xiang-dong, TU Chun-lei, XIE Zong-han. Mechanical properties and fracture mechanism of as-cast MnFeCoCuNi high-entropy alloys [J]. Transactions of Nonferrous Metals Society of China, 2021, 31: 222−231.

[4]   ZHAO Y L, LI Y R, YELI G M, LUAN J H, LIU S F, LIN W T, CHEN D, LIU X J, KAI J J, LIU C T, YANG T. Anomalous precipitate-size-dependent ductility in multicomponent high-entropy alloys with dense nanoscale precipitates [J]. Acta Materialia, 2022, 223: 117480.

[5]   DU Hui, CAI Jia-hong, WANG Ya-song, YAO Jun-qing, CHEN Qiang, CUI Yu, LIU Xin-wang. Effect of partial recrystallization on microstructure and tensile properties of NiFeCoCrMn high-entropy alloy [J]. Transactions of Nonferrous Metals Society of China, 2022, 32: 947−956.

[6]   SENKOV O N, MILLER J D, MIRACLE D B, WOODWARD C. Accelerated exploration of multi-principal element alloys with solid solution phases [J]. Nature Communications, 2015, 6: 6529.

[7]   YANG Jian, ZHOU Ming-Yang, Yang Ji-Jun. Annealing-induced gradient nanostructured FeCrAlTiMo high-entropy alloy coatings with significantly enhanced wear resistance [J]. Tungsten, 2023. https://doi.org/10.1007/s42864-023-00257-7

[8]   GAO Xue-feng, CHEN Rui-run, LIU Tong, FANG Hong-ze, QIN Gang, SU Yan-qing, GUO Jing-jie. High-entropy alloys: A review of mechanical properties and deformation mechanisms at cryogenic temperatures [J]. Journal of Materials Science, 2022, 57(12): 6573−6606.

[9]   ZHANG D D, WANG H, ZHANG J Y, XUE H, LIU G, SUN J. Achieving excellent strength-ductility synergy in twinned NiCoCr medium-entropy alloy via Al/Ta co-doping [J]. Journal of Materials Science & Technology, 2021, 87: 184−195.

[10] FU Yu, LI Jun, LUO Hong, DU Cui-wei, LI Xiao-gang. Recent advances on environmental corrosion behavior and mechanism of high-entropy alloys [J]. Journal of Materials Science & Technology, 2021, 80: 217−233.

[11] KARIMI M A, SHAMANIAN M, ENAYATI M H. Microstructural and mechanical properties assessment of transient liquid phase bonding of CoCuFeMnNi high entropy alloy [J]. Transactions of Nonferrous Metals Society of China, 2021, 31: 3063−3074.

[12] YANG G, KIM J K. Hierarchical precipitates, sequential deformation-induced phase transformation, and enhanced back stress strengthening of the micro-alloyed high entropy alloy [J]. Acta Materialia, 2022, 233: 117974.

[13] QI Yong-liang, CAO Ting-hui, ZONG Hong-xiang, WU Ya-ke, HE Lin, DING Xiang-dong, JIANG Feng, JIN Shen-bao, SHA Gang, SUN Jun. Enhancement of strength−ductility balance of heavy Ti and Al alloyed FeCoNiCr

high-entropy alloys via boron doping [J]. Journal of Materials Science & Technology, 2021, 37: 154−163.

[14] WANG Qiang, ZENG Liang-cai, GAO Teng-fei, DU Hui, LIU Xin-wang. On the room-temperature tensile deformation behavior of a cast dual-phase high-entropy alloy CrFeCoNiAl$_{0.7}$ [J]. Journal of Materials Science & Technology, 2021, 87: 29−38.

[15] YAN Jiao-hui, SONG Zi-jing, FANG Wei, HE Xin-bo, CHANG Ruo-bin, HUANG Shao-wu, HUANG Jia-xin, YU Hao-yang, YIN Fu-xing. Composition design of high yield strength points in single-phase Co-Cr-Fe-Ni-Mo multi-principal element alloys system based on electronegativity, thermodynamic calculations, and machine learning [J]. Tungsten, 2023, 5: 169-178.

[16] WANG Nai-ran, WANG Shou-ren, GOU Xiao-xiang, SHI Ze-cheng, LIN Jian-xiang, LIU Guo-qiang, WANG Yan. Alloying behavior and characterization of (CoCrFeNiMn)$_{90}$M$_{10}$ (M=Al, Hf) high-entropy materials fabricated by mechanical alloying [J]. Transactions of Nonferrous Metals Society of China, 2022, 32: 2253−2265.

[17] ZHANG Zhen, JIANG Zhi-hao, XIE Yue-huang, CHAN S L I, LIANG Jia-miao, WANG Jun. Multiple deformation mechanisms induced by pre-twinning in CoCrFeNi high entropy alloy [J]. Scripta Materialia, 2022, 207: 114266.

[18] EDALATI P, MOHAMMADI A, KETABCHI M, EDALATI K. Microstructure and microhardness of dual-phase high-entropy alloy by high-pressure torsion: Twins and stacking faults in FCC and dislocations in BCC [J]. Journal of Alloys and Compounds, 2022, 894: 162413.

[19] EIßMANN N, MÜHLE U, GAITZSCH U, WALTHER G, WEIßGÄRBER T, KIEBACK B. Precipitation hardening of high entropy alloy CoCrFeMnNi containing titanium [J]. Journal of Alloys and Compounds, 2021, 857: 157610.

[20] TEKIN M, KOTAN H. Microstructural characterization and hardness study of nanostructured CoCrFeNi high entropy alloys with dual effect of Y and nano-sized Y$_2$O$_3$ additions [J]. Transactions of the Indian Institute of Metals, 2022, 75(9): 2389−2394.

[21] SHUN T T, CHANG L Y, SHIU M H. Microstructure and mechanical properties of multiprincipal component CoCrFeNiMo$_x$ alloys [J]. Materials Characterization, 2012, 70: 63−67.

[22] WANG Z G, ZHOU W, FU L M, WANG J F, LUO R C, HAN X C, CHEN B, WANG X D. Effect of coherent L12 nanoprecipitates on the tensile behavior of a fcc-based high-entropy alloy [J]. Materials Science and Engineering: A, 2017, 696: 503−510.

[23] POLAT G, TEKİN M, KOTAN H. Role of yttrium addition and annealing temperature on thermal stability and hardness of nanocrystalline CoCrFeNi high entropy alloy [J]. Intermetallics, 2022, 146: 107589.

[24] TODA C I, JIMÉNEZ J A, MILENKOVIC S, JIMENEZ A J, SAN M D. Microstructural stability of the CoCrFe$_2$Ni$_2$ high entropy alloys with additions of Cu and Mo [J]. Metals, 2021, 11(12): 1994.

[25] FAN A C, LI J H, TSAI M H. On the phase constituents of four CoCrFeNiX (X = Y, Ti, Zr, Hf) high-entropy alloys after prolonged annealing [J]. Journal of Materials Research and Technology, 2020, 9(5): 11231−11243.

[26] WANG Z J, WU Q F, ZHOU W Q, HE F, YU C Y, LIN D Y, WANG J, LIU C T. Quantitative determination of the lattice constant in high entropy alloys [J]. Scripta Materialia, 2019, 162: 468−471.

[27] TEKIN M, POLAT G, KOTAN H. An investigation of abnormal grain growth in Zr doped CoCrFeNi HEAs through in-situ formed oxide phases [J]. Intermetallics, 2022, 146: 107588.

[28] KIRK T, VELA B, MEHALIC S, YOUSEFF K, ARRÓYAVE R. Entropy-driven melting point depression in fcc HEAs [J]. Scripta Materialia, 2022, 208: 114336.

[29] LUAN Heng-wei, SHAO Yang, LI Jin-feng, MAO Wen-lue, HAN Zhi-dong, SHAO Chun-lin, YAO Ke-fu. Phase stabilities of high entropy alloys [J]. Scripta Materialia, 2020, 179: 40−44.

[30] GURUVIDYATHRI K, VAIDYA M, MURTY B S. Challenges in design and development of high entropy alloys: A thermodynamic and kinetic perspective [J]. Scripta Materialia, 2020, 188: 37−43.

[31] TAKEUCHI A, INOUE A. Classification of bulk metallic glasses by atomic size difference, heat of mixing and period of constituent elements and its application to characterization of the main alloying element [J]. Materials Transactions, 2005, 46(12): 2817−2829.

[32] YONG Z, ZUO T T, ZHI T, GAO M C, DAHMEN K A, LIAW P K, ZHAO P L. Microstructures and properties of high-entropy alloys [J]. Progress in Materials Science, 2014, 61: 1−93.

[33] TAKEUCHI A, AMIYA K, WADA T, YUBUTA K, ZHANG W. High-entropy alloys with a hexagonal close-packed structure designed by equi-atomic alloy strategy and binary phase diagrams [J]. JOM, 2014, 66(10): 1984−1992.

[34] TSAI M H, CHANG K C, LI J H, TSAI R C, CHENG A H. A second criterion for sigma phase formation in high-entropy alloys [J]. Materials Research Letters, 2016, 4(2): 90−95.

[35] OTTO F, DLOUHÝ A, PRADEEP K G, KUBĚNOVÁ M, RAABE D, EGGELER G, GEORGE E P. Decomposition of the single-phase high-entropy alloy CrMnFeCoNi after prolonged anneals at intermediate temperatures [J]. Acta Materialia, 2016, 112: 40−52.

[36] ZHANG Lu, HUO Xiao-feng, WANG An-guo, DU Xing-hao, ZHANG Li, LI Wan-peng, ZOU Nai-fu, WAN Gang, DUAN Guo-sheng, WU Bao-lin. A ductile high entropy alloy strengthened by nano sigma phase [J]. Intermetallics, 2020, 122: 106813.

[37] KUBE S A, SCHROERS J. Metastability in high entropy alloys [J]. Scripta Materialia, 2020, 186: 392−400.

[38] QIN Gang, CHEN Rui-run, ZHENG Hui-ting, FANG Hong-ze, WANG Liang, SU Yan-qing, GUO Jing-jie, FU Heng-zhi. Strengthening FCC-CoCrFeMnNi high entropy alloys by Mo addition [J]. Journal of Materials Science & Technology, 2019, 35(4): 578−583.

[39] PARK J M, CHOE J, KIM J G, BAE J W, MOON J, YANG S, KIM K T, YU J H, KIM H S. Superior tensile properties of 1%C−CoCrFeMnNi high-entropy alloy additively manufactured by selective laser melting [J]. Materials Research Letters, 2019, 8(1): 1−7.

[40] KWON H, MOON J, BAE J W, PARK J M, SON S, DO H S, LEE B J, KIM H S. Precipitation-driven metastability

engineering of carbon-doped CoCrFeNiMo medium-entropy alloys at cryogenic temperature [J]. Scripta Materialia, 2020, 188: 140−145.

[41] WU Z, BEI H, PHARR G M, GEORGE E P. Temperature dependence of the mechanical properties of equiatomic solid solution alloys with face-centered cubic crystal structures [J]. Acta Materialia, 2014, 81: 428−441.

[42] ZHU Yun-tian, WU Xiao-lei. Perspective on hetero-deformation induced (HDI) hardening and back stress [J]. Materials Research Letters, 2019, 7(10): 393−398.

[43] MA E, WU X. Tailoring heterogeneities in high-entropy alloys to promote strength−ductility synergy [J]. Nature Communications, 2019, 10(1): 5623.

[44] FEAUGAS X. On the origin of the tensile flow stress in the stainless steel AISI 316L at 300 K: Back stress and effective stress [J]. Acta Materialia, 1999, 47: 3617−3632.

[45] YANG Mu-xin, PAN Yue, YUAN Fu-ping, ZHU Yun-tian, WU Xiao-lei. Back stress strengthening and strain hardening in gradient structure [J]. Materials Research Letters, 2016, 4(3): 145−151.

异质结构 CoCrFeNiW 高熵合金的拉伸性能和强化行为

高雪峰 [1]，陈 峣 [1]，任 浩 [1]，秦 刚 [1]，周启文 [2]，陈瑞润 [1]，郭景杰 [1]

1. 哈尔滨工业大学 金属精密热加工国家重点实验室，哈尔滨 150001；
2. 沈阳工业大学 材料科学与工程学院，沈阳 110870

摘　要：采用真空电弧熔炼方法制备 $Co_{30}Cr_{30}(FeNi)_{40-x}W_x$ (x=0~8% (摩尔分数)，分别简化为 HW0~HW8)高熵合金。研究铸态和退火态合金的显微组织和拉伸性能。结果表明，HW2 和 HW4 具有单一的 FCC 相。随着 W 含量和退火温度的增加，细小粒状 μ 相的面积分数增加且分散在 FCC 基体中。软 FCC 基体和硬 μ 相构成应变不相容的异质结构。随着 W 含量从 0 增加到 8%(摩尔分数)，屈服强度和抗拉强度分别从 278 和 629 MPa 提高到 530 和 839 MPa，应变维持在 33%。退火后的 HW8 表现出优异的屈服强度 (810 MPa) 和抗拉强度 (1087 MPa)。屈服强度的提高归因于固溶、沉淀和背应力强化。异质结构中产生的背应力强化作用诱导高硬化行为，在提高抗拉强度和塑性方面发挥着主导作用。

关键词：高熵合金；异质结构；拉伸性能；应变硬化；强化机制

(Edited by Wei-ping CHEN)